

Effects of a radially varying electrical conductivity on 3D numerical dynamos

Natalia Gómez-Pérez^{*,a}, Moritz Heimpel^b, Johannes Wicht^c

^a*Department of Terrestrial Magnetism, Carnegie Institution of Washington, 5241 Broad
Branch Road N.W., Washington, DC 20015-1305*

^b*Department of Physics, Room 238 CEB, 11322 - 89 Av., University of Alberta, Edmonton,
Alberta, Canada T6G 2G7*

^c*Max Planck Institute for Solar System Research, Max-Planck-Str. 2, 37191
Katlenburg-Lindau*

Abstract

The transition from liquid metal to silicate rock in the cores of the terrestrial planets is likely to be accompanied by a gradient in the composition of the outer core liquid. The electrical conductivity of a volatile enriched liquid alloy can be substantially lower than a light-element-depleted fluid found close to the inner core boundary. In this paper, we investigate the effect of radially variable electrical conductivity on planetary dynamo action using an electrical conductivity that decreases exponentially as a function of radius. We find that numerical solutions with continuous, radially outward decreasing electrical conductivity profiles result in strongly modified flow and magnetic field dynamics, compared to solutions with homogeneous electrical conductivity. The force balances at the top of the simulated fluid determine the overall character of the flow. The relationship between Coriolis and Lorentz forces near the outer boundary controls the flow and magnetic field intensity and morphology of the system. Our results imply that a low conductivity layer near the top of Mercury's liquid outer core is consistent with its weak magnetic field.

Key words: Variable electrical conductivity, numerical dynamos, Geodynamo, Mercury

1. Introduction

Variations in the physical properties of fluids in planetary dynamos define the character of the observed intrinsic magnetic field (e.g., strength, geometry and time variability). Changes in the electrical conductivity of the fluid as a function of depth may become relevant in the context of terrestrial and gas giant

*Corresponding author

Email address: ngomezperez@ciw.edu (Natalia Gómez-Pérez)

planets. In this paper we explore (with a focus on the terrestrial planets) how the radial variation of electrical conductivity in planetary cores may result in changes to dynamo-generated magnetic fields.

1.1. Terrestrial planets

The cores of the terrestrial planets are composed principally of iron, with minor but significant amounts of nickel and lighter elements. It has long been known that an iron-nickel core would have too high a density to be compatible with Earth's moment of inertia and seismic data (e.g., Birch, 1952; Poirier, 1994). A compatible Earth core density model can result from the inclusion of about 8% by weight of one or more light elements. Detailed models of core composition are based primarily on the constraints of seismology, mineral physics, geochemistry, metallurgy, and cosmochemistry. Silicon, sulphur and oxygen are the primary candidates for the light elements. Sulphur is likely to be a significant component but the depletion of light elements in the process of accretion in the inner solar system limits sulphur to about 2 wt% in the core.

Recent reviews of core differentiation and composition distinguish between models considering Silicon versus those considering Oxygen as the primary light element. Composition models give weight percents of Fe \simeq 85%-88%, Ni \simeq 5% Si \simeq 0-7%, O \simeq 0-4% and S \simeq 2% (e.g McDonough, 2003; Wood et al., 2006). Solidification of a more or less pure iron-nickel inner core may exclude the lighter elements, which would then be enriched in the outer core. The ratio of the inner core radius (1221 km) to the core radius (3480 km) is 0.35 and the mass of the inner core is only about 5% of the total core mass. So the bulk composition of the outer core is only slightly different than that of the whole core.

Convection in the liquid outer core is driven by a combination of compositional and/or thermal buoyancy. Thermal buoyancy available to drive convection and dynamo action originates primarily from the latent heat of solidification at the inner core boundary (ICB) and possibly from cooling at the core-mantle boundary (CMB). Secular cooling at the CMB does not guarantee a source of convective instability since heat can be conducted through a stably stratified layer (a super-adiabatic heat flux is needed). Compositional buoyancy originates at the ICB due to light element enrichment in the residual liquid associated with inner core solidification. A source of compositional buoyancy near the CMB could come from precipitation from a silicate enriched layer at the top of the core, leaving a light element depleted, heavy residual liquid and a silicate sediment layer at the CMB (Buffett et al., 2000).

Temperature and pressure dependence of electrical conductivity may lead to sizable variations with depth. (Stacey and Anderson, 2001). Assuming a well-mixed outer core and a Si concentration of $X_{Si} = 0.25$ in a dual species alloy, the authors found the most extreme variation in the fluid core of Earth results in a factor of 1/2 difference for the electrical conductivity and about 3/4 for the thermal conductivity from the ICB to the CMB. Although the effects of different impurities in the alloy have not been explored experimentally, Stacey and Anderson (2001) argue that the effects of impurities other than Si do not significantly change their estimates. A later revision (Stacey and Loper, 2007)

found that the variation in electrical and thermal conductivities had been over-estimated due to the assumption of treating Fe as an electronically simple metal. Their later results predict a difference in the electrical conductivity of a factor of 0.78 between that of the CMB when compared to the ICB's. Those estimates were made under the assumption of a well-mixed outer core. However gradients in material properties would be amplified in a compositionally stratified layer.

The existence of a thermally and/or compositionally stably stratified layer near the top of the Earth's core has been both, suggested and argued (Jacobs, 1975; Fearn and Loper, 1981; Lister and Buffett, 1998; Braginsky, 1993, 2007). Here we will focus on the possibility of a compositionally stratified layer near the top of the core since the electrical conductivity in such a layer would decrease with radius (due to the higher light-element concentration when compared to the bottom of the fluid core). Two mechanisms by which a compositionally stratified layer can grow are by chemical diffusion from the mantle directly to the top of the core (Lister and Buffett, 1998) and by buoyant transport of light element enriched residual liquid from inner core solidification (Moffatt and Loper, 1994). Chemical diffusion is a slow process and would not result in a layer thickness greater than about 10 km (Lister and Buffett, 1998). On the other hand, buoyant rise of light element rich residual liquid could be an efficient process to build a layer of greater thickness. A thick layer with a significantly anomalous density would likely be detected as a seismically fast layer. Seismological constraints have been so far inconclusive. However, recent seismological results using outermost core waveforms seem to be consistent with the existence of a low density layer of about 100 km thickness (Alexandrakis and Eaton, 2007; Tanaka, 2007)

It has been confirmed that Mercury has a liquid iron core (Margot et al., 2007). Furthermore, it is likely that Mercury's weak intrinsic magnetic field is generated by a dynamo in its liquid outer core. Neither the details of Mercury's core composition, nor the size of its inner core is known (Hauck et al., 2004; Solomon et al., 2008; Heimpel and Kabin, 2008). Observations of Mercury's contractional lobate crustal faults imply a planetary radial contraction of about 3 km, small compared to an estimated 17 km of contraction that would result from a completely solidified core. This implies that Mercury may have a relatively large outer core, perhaps earth-like proportion. For a thick-shell outer core to exist in Mercury, given its small size, Hauck et al. (2004) estimates that the light elements (such as S or Si) in the core have a relatively high concentration. This suggests the possibility of a large and stratified Hermean outer core with a thick, and stably stratified outermost layer. Such a layer would be compositionally stratified (in contrast to thermally stratified models previously proposed, e.g., Christensen, 2006) with a radial increase in the proportion of a light elements, and a radial decrease in electrical conductivity.

1.2. Gas giant planets

The magnetic field in the gas giants is generated within a metallic hydrogen region. Experimental results have found that the transition from metallic to

molecular hydrogen yields a wide range of pressures where the electrical conductivity is non-negligible thus varying slowly with depth in planetary interiors (Nellis, 2000). The internal structure has been deduced to first order based on measurements of the moment of inertia and total mass of each planet (e.g., Guillot, 2005). However, constraints on hydrogen and helium mixtures at high pressures need to be found in order to better determine the internal structure of the gas giants. The additional effect of helium may complicate further the underdetermined internal layering of gas giants (e.g., Stevenson, 2008). The metallic to molecular hydrogen transition is of particular interest from the point of view of the internal dynamics. The depth and radial extent of this transition are important for magnetic field generation and in understanding the observable magnetic field morphology. This is a task for future investigation.

In this paper, we present results from a numerical dynamo model with radially varying electrical conductivity (Gómez-Pérez, 2007). To implement the radially variable conductivity, we modified an existent numerical code (originally MagIC 2.0, Wicht, 2002), that uses the Boussinesq approximation. We focus this study on the effect of the varying conductivity on the dynamo action, and on the generated magnetic field. With this new implementation we performed a set of tests to analyze its consistency with previously published work. In section 2 we include a review of numerical models that worked with stratified liquids. In section 3 we present the necessary modification to the dynamo equations, and to the numerical code. The parameters explored for twenty runs studied in this paper are included in section 4. We present the results in section 5, the discussion and conclusions are found in section 6 and 7, respectively. We also included a table of symbols in appendix A.

2. Stratified planetary interiors in numerical simulations

The study of planetary and solar dynamos has evolved rapidly in the past two decades due to code development and the accessibility to powerful computers used to solve numerically the equations of motion of rotating fluids. Solutions of numerical dynamos share characteristics with Earth’s dynamo with respect to temporal variability, evolution and mean geometry (e.g., Kageyama et al., 1993; Glatzmaier and Roberts, 1995; Kuang and Bloxham, 1997; Christensen et al., 1998). More recently, numerical models have been successful in reproducing non-dipolar and weak fields such as those observed for the ice giants (e.g., Gómez-Pérez and Heimpel, 2007; Stanley and Bloxham, 2006). Nevertheless, these models of planetary dynamos rely on strong assumptions that do not necessarily represent realistic physical conditions expected for planetary interiors. For example, due to hardware limitations, numerical models cannot simultaneously resolve planetary- and small-scale flow, both of which are prevalent for low viscosity fluids such as liquid iron or metallic hydrogen in a planetary setting.

2.1. Buoyancy stratification

Christensen and Wicht (2008), and Christensen (2006) implemented a stable stratified (non-convecting) layer at the top of the electrical conductive fluid in

planetary dynamo models. They showed that small scale magnetic fields, may be generated in the deep interior of the electrically conductive fluid, shielded by a stably stratified layer. This outer layer acts as a filter that mainly damps the rapidly varying small scale components by the magnetic skin effect. They conclude that the axisymmetric field of Saturn and the relatively weak field of Mercury may be explained by a stably stratified layer at the top of the dynamo region. Similarly, Stanley and Mohammadi (2008) using buoyantly stratified fluids, found that zonal winds developed in a stable layer can affect the magnetic field time evolution rendering a secular variation of thermally stratified models inconsistent with Earth’s observed field.

2.2. Density stratification

We discuss briefly the effects of density variation (anelastic versus Boussinesq approximations) in this section, since they are closely linked to those of the electrical conductivity. In order to solve the anelastic dynamo equations numerically, Glatzmaier (1984) used a poloidal and toroidal decomposition for the velocity and magnetic fields (for the decomposition of solenoidal vectors the reader may refer to Chandrasekhar, 1961). This allows for the use of a pseudo-spectral algorithm, which has been extensively used in planetary and solar dynamo simulations (e.g., Glatzmaier, 1984; Dormy et al., 1998; Christensen et al., 1999; Sakuraba and Kono, 1999; Clune et al., 1999). This mathematical approach requires field vectors to be solenoidal (i.e., divergence free) and thus, approximations are used for the continuity equation, $\nabla \cdot (\rho \mathbf{u}) + \partial \rho / \partial t = 0$, where \mathbf{u} is the velocity, ρ the density of the fluid and t is time. If the time scale of convection is large compared to the time for sound waves to travel across the depth of the shell, then $\partial \rho / \partial t \ll \nabla \cdot (\rho \mathbf{u})$ and the anelastic approximation, $\nabla \cdot (\rho \mathbf{u}) = 0$, is obtained. In addition, if the density changes in the fluid are much smaller than the averaged density, one obtains the Boussinesq approximation, $\nabla \cdot \mathbf{u} = 0$, where the buoyancy is determined by temperature changes exclusively, but the density perturbations with respect to the mean are neglected.

Differences between the results obtained using Boussinesq and anelastic approximations have been compared in the context of magnetic convection in 2D models (Evonuk and Glatzmaier, 2004). They find significant effects due to strong density stratification (about three orders of magnitude variation in density). The length scales of the top and bottom thermal plumes differ due to the compressibility of the liquid. 3D effects on the flow are very significant as well, and although the effect on the density variation is likely to be important in three-dimensional systems, a detailed analysis of density variations in 3D flows needs to be completed.

Anufriev et al. (2005) compared Boussinesq and anelastic approximations analytically and found that they differ in the thermodynamic equations. In the latter, the rate of work to expand or contract the fluid is included in the energy balance, while the Boussinesq treats a thermal balance as the total energy balance. The anelastic approximation takes into account a more complete picture by including cooling or heating done by the flow. They propose a change in the

thermal boundary conditions in Boussinesq models in order to allow for a realistic energy balance in the system. This suggestion should be seriously considered in future numerical simulations that use the Boussinesq approximation.

We are not aware of previous numerical simulations that studied the effects of varying electrical conductivities in the context of planetary interiors. Anelastic models of the interior of stars include variations on magnetic and viscous diffusivities, and thermal expansion coefficient changing as a function of background density, $\propto \bar{\rho}^{-1/2}$ (Featherstone et al., 2007; Clune et al., 1999). Their numerical models include high resolution runs, specially targeted for stellar dynamos (e.g., the heat transport throughout the simulated volume is set up to follow hydrogen burning at the deep interior). Here, we study the effects of radially varying electrical conductivity on the flow and on the magnetic field generation in the liquid cores of terrestrial planets.

3. Methodology

3.1. Governing equations

To describe the behavior of an electrically conductive fluid bounded by co-rotating spherical shells, we use the magnetohydrodynamic equations in the frame of the rotating fluid. Consider a spherical shell with inner and outer boundary radii r_i and r_o respectively, rotating with an angular velocity $\boldsymbol{\Omega}$. Using the Boussinesq approximation, these equations are written as:

$$E \left(\frac{\partial \mathbf{u}}{\partial t} + (\mathbf{u} \cdot \nabla) \mathbf{u} - \nabla^2 \mathbf{u} \right) + 2\hat{\mathbf{z}} \times \mathbf{u} = -\nabla P + \frac{RaE}{Pr} \frac{g}{g_o} \hat{\mathbf{r}} T + \frac{1}{Pm^*} (\nabla \times \mathbf{B}) \times \mathbf{B}, \quad (1)$$

$$\nabla \cdot \mathbf{u} = 0, \quad \nabla \cdot \mathbf{B} = 0, \quad (2)$$

$$\frac{\partial T}{\partial t} + \mathbf{u} \cdot \nabla T = \frac{1}{Pr} \nabla^2 T, \quad (3)$$

$$\frac{\partial \mathbf{B}}{\partial t} = \nabla \times (\mathbf{u} \times \mathbf{B}) - \frac{1}{Pm^*} \nabla \times (\tilde{\lambda} (\nabla \times \mathbf{B})), \quad (4)$$

where \mathbf{u} and \mathbf{B} are the velocity and magnetic induction vectors, respectively; t is time; T and P are the temperature and pressure scalars, respectively; g is the acceleration of gravity which changes linearly with depth, and g_o is the value of this acceleration at the outer boundary; $\hat{\mathbf{r}}$ is the radial unit vector, and $\hat{\mathbf{z}}$ is the unit vector in the direction of the angular momentum of the rotating frame. $\tilde{\lambda}(r) = \frac{\lambda(r)}{\lambda_i}$ is the normalized magnetic diffusivity, where $\lambda(r)$ and $\lambda_i = \lambda(r_i)$ are the magnetic diffusivities, in units of m^2s^{-1} , of the liquid core as a function of r and of the solid inner core respectively.

Equations 1 to 4 are expressed in terms of the following non-dimensional parameters: the Rayleigh number,

$$Ra = \frac{\alpha g_o \Delta T D^3}{\kappa \nu}, \quad (5)$$

where α is the thermal expansion coefficient and κ is the thermal diffusivity. The Ekman number,

$$E = \frac{\nu}{\Omega D^2}, \quad (6)$$

which is the ratio between viscous and Coriolis forces in the system. The Prandtl number,

$$Pr = \frac{\nu}{\kappa}, \quad (7)$$

which is the ratio between the viscous and the thermal diffusivities. And a modified magnetic Prandtl number,

$$Pm^* = \frac{\nu}{\lambda_i}, \quad (8)$$

which is the ratio between the viscous diffusivity of the fluid and the magnetic diffusivity at the inner boundary, $\lambda(r_i) = \lambda_i$. Note that the magnetic Prandtl number changes as a function of radius, we used the maximum magnetic Prandtl number for the definition of the non-dimensional units used in our numerical model.

The second term in the right hand side of equation 4 may be written as:

$$\frac{1}{Pm^*} \nabla \times (\tilde{\lambda}(\nabla \times \mathbf{B})) = \frac{1}{Pm^*} \left[-\tilde{\lambda} \nabla^2 \mathbf{B} + \nabla \tilde{\lambda} \times (\nabla \times \mathbf{B}) \right], \quad (9)$$

in which the variable conductivity modifies the term $\nabla \tilde{\lambda} \times (\nabla \times \mathbf{B})$ exclusively.

The magnetic induction equation is modified by the spatial variability of $\lambda(r)$. Since \mathbf{B} is solenoidal, we define the magnetic field as a function of two scalar potentials (see Chandrasekhar, 1961, Appendix III):

$$\mathbf{B} = \nabla \times \nabla \times \Phi \hat{\mathbf{r}} + \nabla \times \Psi \hat{\mathbf{r}}, \quad (10)$$

where Φ is the toroidal and Ψ the poloidal potential. From this decomposition the time variation of the potentials (Gómez-Pérez, 2007):

$$\frac{L_H}{r^2} \frac{\partial \Phi}{\partial t} = \hat{\mathbf{r}} \cdot (\nabla \times (\mathbf{u} \times \mathbf{B})) + \frac{\tilde{\lambda}}{Pm^*} \frac{L_H}{r^2} \left[\frac{\partial^2}{\partial r^2} - \frac{L_H}{r^2} \right] \Phi. \quad (11)$$

$$\begin{aligned} \frac{L_H}{r^2} \frac{\partial \Psi}{\partial t} &= \hat{\mathbf{r}} \cdot \nabla \times (\nabla \times (\mathbf{u} \times \mathbf{B})) \\ &+ \frac{\tilde{\lambda}}{Pm^*} \frac{L_H}{r^2} \left[\frac{\partial^2}{\partial r^2} - \frac{L_H}{r^2} \right] \Psi + \frac{\nabla_r \tilde{\lambda}}{Pm^*} \frac{L_H}{r^2} \frac{\partial \Psi}{\partial r}, \end{aligned} \quad (12)$$

where $\nabla_r = \hat{\mathbf{r}} \cdot \nabla$. It is convenient to write the horizontal component of the angular momentum operator as $L_H = -r^2 \nabla_H$, with $\nabla_H = \nabla - \nabla_r$. The term $-\lambda \nabla^2 \mathbf{B}$ in equation 9 introduces a zero order effect of a varying electrical diffusivity, it results on a decrease of the ohmic dissipation with depth, for both, poloidal and toroidal components of the magnetic field. The radial derivative of the diffusivity has a first order effect, involving exclusively the poloidal component. This is controlled by the term $\nabla \tilde{\lambda} \times (\nabla \times \mathbf{B})$ in equation 9.

3.2. Radially variable electrical conductivity

The radial change in electrical conductivity, $\sigma(r) = \frac{1}{\mu_0 \lambda(r)}$, where μ_0 is the magnetic permeability of vacuum, is modeled with a piecewise continuous function whose derivative is also continuous. The outermost part decreases exponentially while the interior changes as a power of the radius. One may write the normalized electrical conductivity as:

$$\tilde{\sigma}(r) = \begin{cases} 1 + (\tilde{\sigma}_m - 1) \left(\frac{r - r_i}{r_m - r_i} \right)^a, & r < r_m \\ \tilde{\sigma}_m \exp \left[\frac{k}{\tilde{\sigma}_m} (r - r_m) \right], & r \geq r_m \end{cases} \quad (13)$$

where r_i is the inner boundary, r_m is the radius where were the electrical conductivity changes from a polynomial to an exponential function, a determines how fast the exponential function decreases outside the conductive volume, $\tilde{\sigma}_m$ is chosen to be the value of the normalized conductivity where the functions match, $\tilde{\sigma}(r_m) = \tilde{\sigma}_m$, and $k = a(\tilde{\sigma}_m - 1)(r_m - r_i)^{-1}$ (see figure 1). We choose to implement a continuous differentiable function in order to have an analytical solution for λ and $\nabla \lambda$. This function for the electrical conductivity is chosen to model a layering between an light-element-enriched fluid with a light-element-poor fluid. During the solidification of the core, heavy elements are preferentially deposited on the inner core. As a result, light element enriched liquid rises buoyantly to the top of the outer core, just below the CMB. A more realistic representation of the electrical conductivity variability, and of miscibility of iron and light element enriched iron at high pressures, needs to be studied. From an experimental point of view such measurements are very challenging. First principles numerical simulations (e.g., Caracas and Verstraete, 2009) may lead to some useful results and a more realistic characterization of $\lambda(r)$ may be implemented in the future.

4. Dynamo regimes studied

We study self-sustained dynamos in two main regimes. First, we include two sets of cases with relatively low Ra , where the resultant fields are non-reversing and dipole dominated. Second, we analyzed strongly forced and time variable cases where dynamos result in dipolar magnetic fields with strong multipolar components. We chose a values for $Ra = 3.4Ra_c = 2.5 \times 10^6$ (set A), $Ra = 7.8Ra_c = 8.5 \times 10^7$ (set B) and $Ra = 16.8Ra_c = 1.3 \times 10^7$ (sets C and C'), where the value of Ra_c was calculated using the empirical formula for the onset

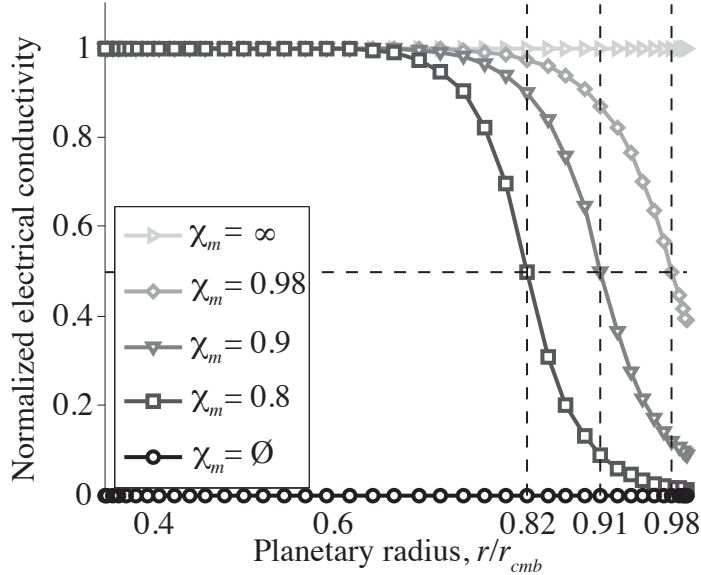


Figure 1: Normalized electrical conductivity as a function of radius. The electrical conductivity is normalized with the conductivity of the inner core. r_m was chosen to be a grid point and thus $\chi_m = 0.91 \approx 0.9$ and $\chi_m = 0.82 \approx 0.8$ are labelled in the text as $\chi_m = 0.9$ and $\chi_m = 0.8$ respectively.

of convection in rotating spherical shells from Al-Shamali et al. (2004). For sets A, C and C', $E = 10^{-4}$ and $E = 10^{-5}$ for set B. Common parameters used for all sets are a Prandtl number $Pr = 1$, and a radius ratio $\chi = \frac{r_i}{r_o} = 0.35$. For sets A, B and C non-slip and fixed temperature boundary conditions are used at both, bottom and top boundaries. We also include cases with top and bottom free-slip boundaries, i.e., set C'. For this set, all other parameters identical to those of set C. The models account for an electrically conductive inner core where electrical conductivity is homogeneous in the inner core, continuous through the ICB, and may vary radially in the outer core. The electrical conductivity for the mantle was chosen to be zero. All simulations in sets A, C and C' have the same resolution, with 61 radial levels for the outer core and 17 for the inner core; 288 ($l_{max} = 120$) grid points in the azimuthal direction and half of that in the latitudinal direction. For set B the latitudinal and azimuthal resolution was increased to 256 and 512 respectively ($l_{max} = 170$) and 65 radial levels were used. Hyperdiffusivities were not used for any of the runs presented in this paper. For the purpose of normalization only, the magnetic Prandtl number, $Pm^* = 5$, is defined by the ratio between the viscous diffusivity of the fluid, ν , and electrical diffusivity of the inner core, λ_i (which is the minimum diffusivity in the simulated volume).

For each set A, B, C and C' we compare two cases with homogeneous elec-

trical conductivity in the fluid with cases with electrical conductivity varying as a function of radius. To label these cases $\chi_m = r_m/r_o$ is used, where r_m is the same used in equation 13. Cases with homogeneous conductivity are: non-magnetic case (from here on referred to as $\chi_m = \emptyset$) and a case with constant electrical conductivity ($\chi_m = \infty$). The radially variable electrical conductivity cases A, B, C and C' have $\chi_m \approx 0.8$, $\chi_m \approx 0.9$ and $\chi_m \approx 0.98$, see figure 1. The shape of the electrical conductivity function is defined by equation 13. For all cases $a = 10$, and $\tilde{\sigma}_m = \frac{1}{2}$.

5. Results

Significant changes in the internal dynamics of the simulations are obtained by varying the electrical conductivity profile. Energy time series for sets A and C are included in figures 2 and 3. The time variability of the solution varies with χ_m . We find quasi-stationary solutions for set A for $\chi_m = 0.8$ and $\chi_m = 0.9$. The solutions for sets B, C and C' did not result in quasi-stationary solutions, as may be seen for set C in figure 3.

We include Table 1 with time-averaged values, where the average has been taken over two viscous diffusion times. The standard deviation from the time-averaged value is also included.

The Reynolds number, $Re = \frac{\langle |\mathbf{u}| \rangle D}{\nu}$, for $\chi_m = \emptyset$ is always greater than for the corresponding $\chi_m = \infty$. In particular, the toroidal kinetic energy is decreased due to the presence of Lorentz forces.

Values of the averaged Elsasser number, $\Lambda = \frac{\langle \mathbf{B}^2 \rangle}{\rho \mu_0 \lambda_i \Omega}$ in the fluid outer core and at the top of the simulated fluid are included in columns four and five in Table 1. It is important to note that the definition of Λ uses λ_i instead of $\lambda(r)$ to be consistent with the normalization and the non-dimensional parameters. Using the total magnetic energy, M , the axisymmetric dipolar magnetic energy, M^a , and the total and axisymmetric energy at the CMB, M_o , and M_o^a , respectively; we calculate the ratio of the axisymmetric dipole to the whole magnetic energy for the whole fluid ($Q^a = M^a/M$) and at the CMB ($Q_o^a = M_o^a/M_o$). These values are shown in columns 7 and 6, respectively.

The axisymmetric dipole component is dominant for all runs in set A, see Q_o^a in column six in Table 1. In contrast, the magnetic field energy is distributed over higher multipoles in sets B, C, and C', due to the higher Ra/Ra_c value. For these three sets, the variable conductivity cases exhibit broader length scale features and weaker fields at the CMB than case $\chi_m = \infty$, this is due to the diffusion of magnetic field through the low electrical conductivity volume.

Observable characteristics of dynamos are limited to the radial component of the magnetic field at the CMB and its temporal variability. It is important to understand how the flow dynamics is correlated to the surface field. Quantities such as Q_o^a in Table 1 serve as an indication of the observable magnetic field. In contrast, Q^a characterizes how the magnetic field being carried by the core flow behaves. We compare how much of the fluid core axisymmetry is carried to the CMB surface field. To do this, we take the ratio of the normalized

Table 1: Time-averaged values for all cases studied in this paper. In the first and second columns the ratios Ra/Ra_c and $\chi_m = r_m/r_o$. Columns three and four, the time-averaged mean Reynolds, Re , and Elsasser Λ numbers. In column five, the mean Elsasser, Λ^{CMB} , number at the top boundary. In columns six and seven the ratios of axial dipole energy to total field energy at the CMB (Q_o^a), and for the fluid outer core (Q^a) respectively. Note that the values presented for the magnetic field at $r = r_o$ are the sum of both, poloidal and toroidal components, as opposed to only poloidal (corresponding to the external field). Lastly, in columns eight and nine, the time- and space-averaged Hartmann and thermal boundary layer thicknesses, δ_H and δ_k .

Ra/Ra_c	χ_m	Re	Λ	Λ^{CMB}	Q_o^a	Q^a	δ_H	δ_k
3.4	0.00	133.5±9.5						0.3575±0.0022
3.4	0.80	121.7±6.1	3.8±0.2	0.029±0.001	0.78±0.01	0.0565±0.0036	0.114659±0.006442	0.3554±0.0014
A	3.4	0.90	118.6±4.5	7.5±1.2	0.026±0.001	0.0257±0.0057	0.050601±0.001241	0.3497±0.0029
3.4	0.98	123.2±7.0	23.0±4.2	0.250±0.100	0.61±0.10	0.0513±0.0126	0.003315±0.001058	0.3266±0.0117
3.4	∞	109.6±9.5	36.4±6.8	1.055±0.272	0.60±0.06	0.1224±0.0195	0.000483±0.000129	0.3228±0.0163
7.8	0.00	638.7±23.1						0.2355±0.0023
B	7.8	0.80	542.6±34.2	67.6±8.1	0.120±0.043	0.05±0.07	0.006126±0.002463	0.1726±0.0155
7.8	0.90	505.8±32.1	99.1±11.9	0.403±0.134	0.01±0.01	0.0014±0.0009	0.001160±0.000463	0.1604±0.0135
7.8	0.98	360.4±27.6	387.4±56.0	20.269±4.161	0.43±0.07	0.1095±0.0170	0.000005±0.000001	0.1514±0.0102
7.8	∞	360.1±31.9	447.7±102.7	34.748±11.645	0.32±0.07	0.1105±0.0212	0.000002±0.000001	0.1572±0.0141
16.8	0.00	814.1±31.4						0.0974±0.0043
16.8	0.80	704.0±32.3	39.9±4.2	0.042±0.010	0.04±0.05	0.0014±0.0009	0.413985±0.155259	0.0990±0.0047
C	16.8	0.90	662.3±29.9	65.8±5.5	0.329±0.060	0.02±0.02	0.0016±0.0011	0.032156±0.008828
16.8	0.98	661.0±30.0	66.5±6.1	0.335±0.063	0.02±0.03	0.0016±0.0012	0.015181±0.004695	0.0984±0.0046
16.8	∞	506.8±27.2	336.3±30.2	22.479±2.637	0.13±0.02	0.0375±0.0059	0.000073±0.000010	0.1020±0.0054
16.8	0.00	1646.0±66.1						0.1664±0.0261
16.8	0.80	1485.3±24.7	66.5±7.0	0.096±0.029	0.04±0.05	0.0018±0.0012	0.132790±0.057043	0.1277±0.0099
C'	16.8	0.90	883.8±33.7	103.8±9.0	0.480±0.110	0.01±0.02	0.0015±0.0009	0.019941±0.005702
16.8	0.98	753.7±33.2	117.4±8.8	1.258±0.238	0.01±0.01	0.0015±0.0010	0.006946±0.001642	0.1023±0.0066
16.8	∞	627.4±33.2	276.7±35.7	9.576±2.099	0.20±0.03	0.0329±0.0074	0.000143±0.000040	0.1008±0.0060

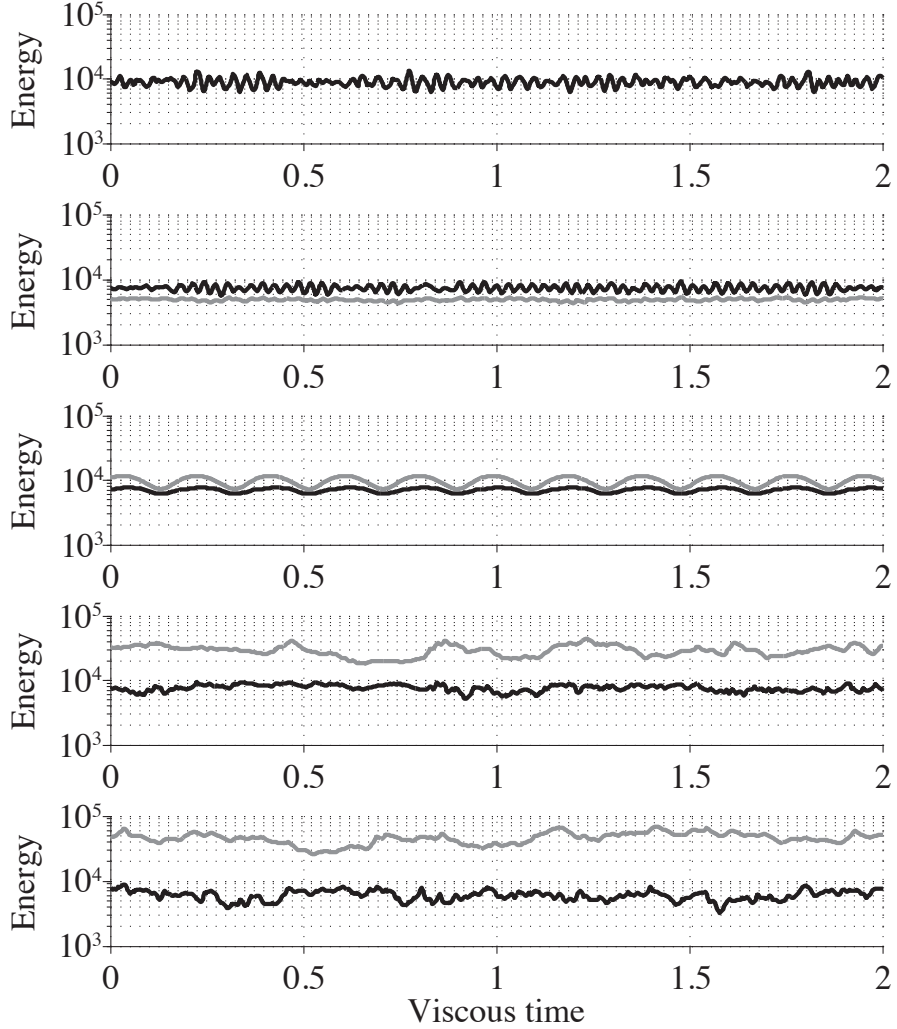


Figure 2: For set A, time series of the total kinetic energy in the fluid (in back) and the total magnetic energy (in grey). From top to bottom increasing values of χ_m ; $\chi_m = \emptyset$, $\chi_m = 0.8$, $\chi_m = 0.9$, $\chi_m = 0.98$, and $\chi_m = \infty$ in rows one to five.

surface axisymmetric dipole energy and the normalized fluid core axisymmetric dipole energy, this quantity is shown as a function of χ_m in figure 4. With the exception of set A a tendency for decreasing Q_o^a/Q^a is found for increasing χ_m . This is reasonable since higher harmonics are preferentially damped by the diffusion through the non-conducting volume. Thus, models with larger non-conductive volumes result in stronger axisymmetric dipoles at the top surface. The exception to this in set A is given by the average of $\chi_m = 0.9$, the quasi-

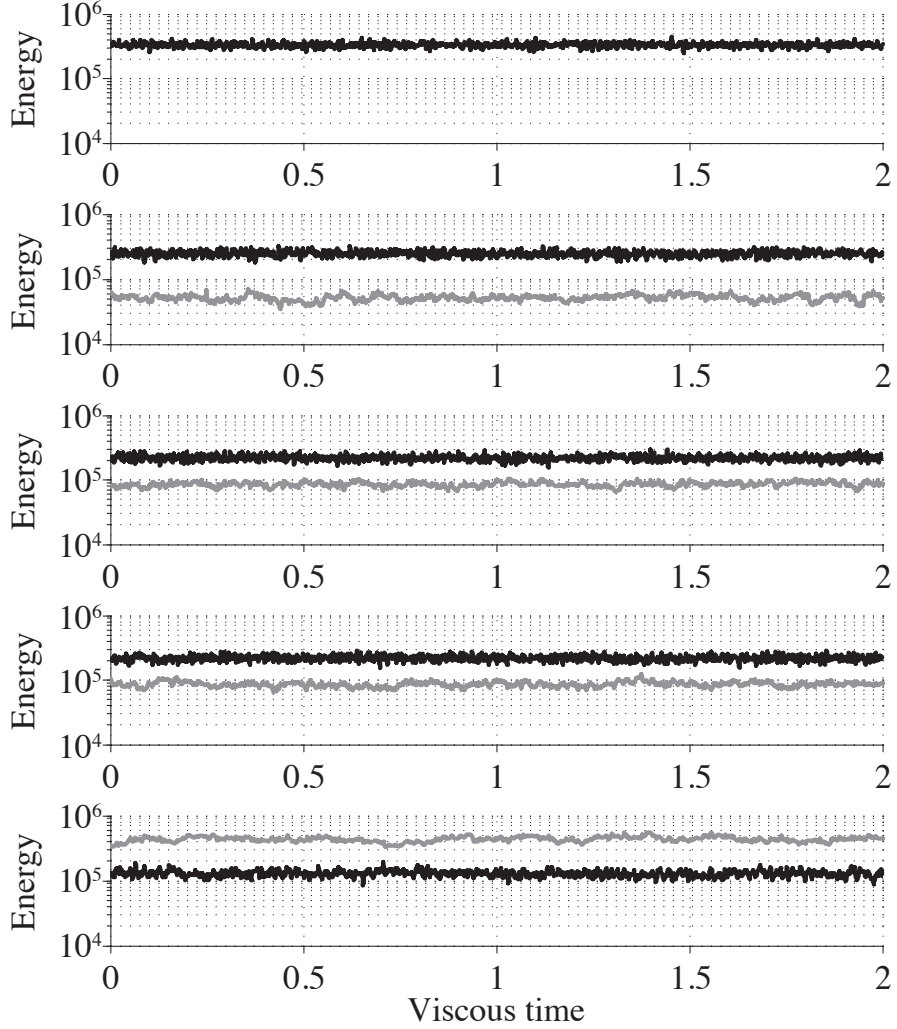


Figure 3: Similar to figure 2 but for set C. $\chi_m = 0$, $\chi_m = 0.8$, $\chi_m = 0.9$, $\chi_m = 0.98$, and $\chi_m = \infty$ in rows one to five.

stationary solution results in an increased axisymmetry when compared to $\chi_m = 0.8$. It is possible that this is a consequence of the periodic variation (see panel 3 in figure 2) reinforcing and stabilizing the axisymmetric components of the magnetic field.

In figure 5 equatorial profiles of the temperature field are shown. A behaviour change is evident between the homogeneous non-magnetic and magnetic solu-

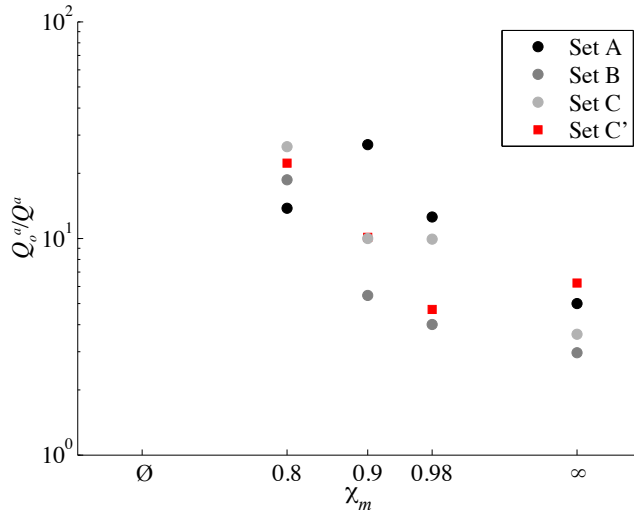


Figure 4: Time average of the ratio of the relative axisymmetric dipole energy at the CMB (Q_o^a) and the relative axisymmetric dipole energy over the fluid core (Q^a). The ratio has been calculated for all runs where magnetic fields are non-zero and the color refers to sets A (Black), B (dark grey), and C (light grey). Values of simulations in set C' are shown with red squares.

tions, with the variable conductivity solutions as intermediate states. For set A, columns one to three ($\chi_m = \emptyset, 0.8, 0.9$) exhibit a similar behaviour. The presence of a mean zonal flow bending the hot thermal plumes in the prograde direction is visible, while for the fifth column ($\chi_m = \infty$) there is no evidence for a strong axisymmetric zonal flow, and the plumes have a dominant radial direction. Column four ($\chi_m = 0.98$) shows a weak prograde tilt. For set B, a transition is seen between $\chi_m = 0.9$ and $\chi_m = 0.98$, although there is also a significant morphology difference between the non-magnetic case and the variable conductivity $\chi = 0.8$ and $\chi_m = 0.9$. For the third row (set C) there is a difference between the finite χ_m runs and $\chi_m = \infty$ in the characteristic azimuthal wave number of the plumes. In $\chi_m = \infty$ of set C there are six distinguishable hot plumes while for all others the wave number is as high as nine.

In figure 6, snapshots (at the same instants as for figure 5) of equatorial profiles of the axial vorticity are shown. Corresponding equatorial profiles of $|\mathbf{B}|$ in figure 7 are included for all sets.

In set A there is a clear correlation between the cyclonic vortices (in black) with the magnetic field magnitude maxima (in white). Similarly to the temperature, the wave number of the vorticity profiles of the variable conductivity cases is equal to that of the non-magnetic case and allows for smaller scale features. For set A, as well as seen in the temperature profiles, the presence of zonal flow bends the vortices in a prograde direction. Runs with $\chi_m = 0.8$ and $\chi_m = 0.9$

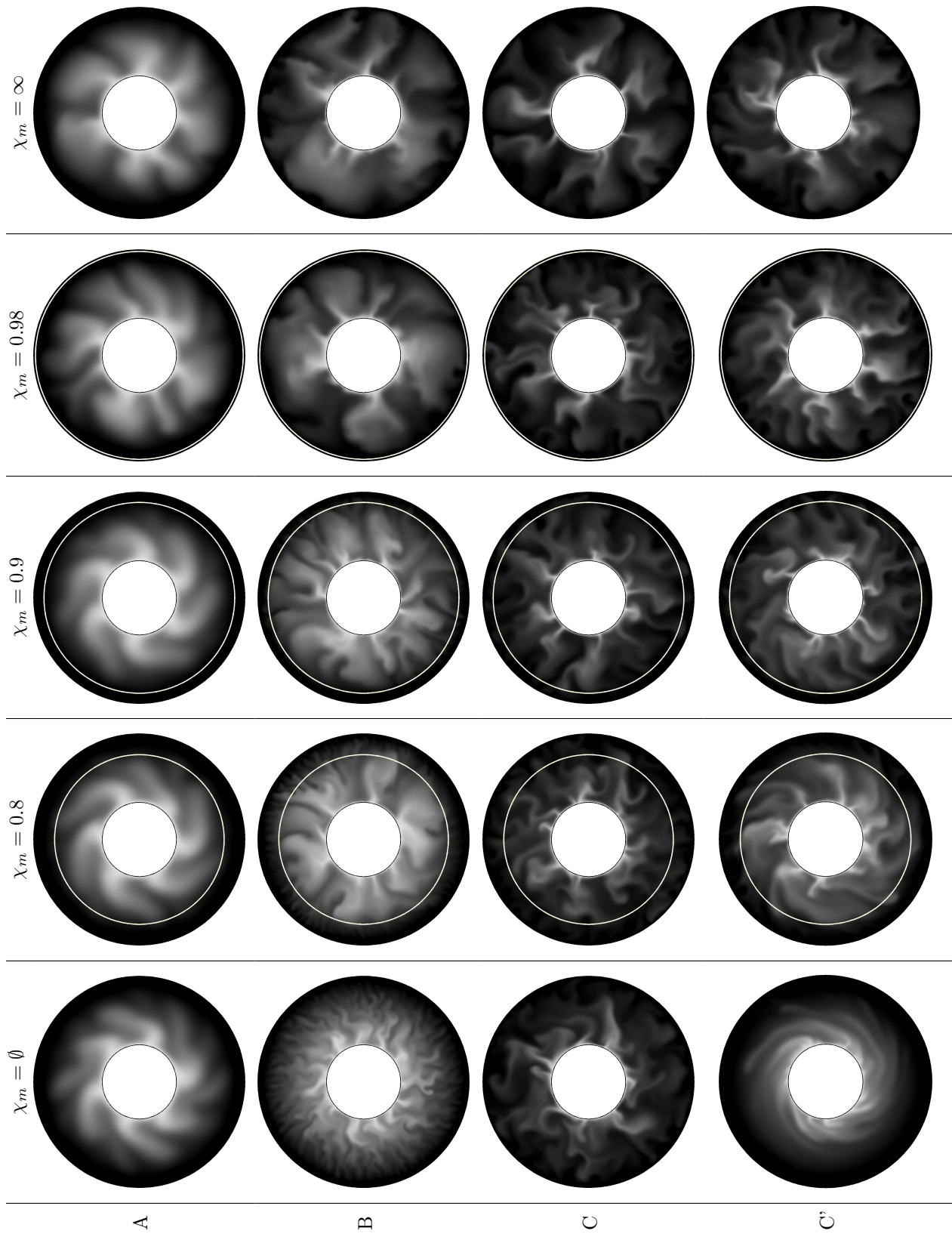


Figure 5: Panels show randomly chosen snapshots of the equatorial temperature for the models for set A, B, C and C' from top to bottom rows. From left to right: non-magnetic convective cases, variable conductivity models with $\chi_m = 0.8$ and $\chi_m = 0.9$, $\chi_m = 0.98$, and homogeneous non-zero electrical conductivity solutions. For the variable conductivity cases the circle of radius r_m is shown with a white solid line. All panels show the normalized temperature from 0 (black) to 1 (white).

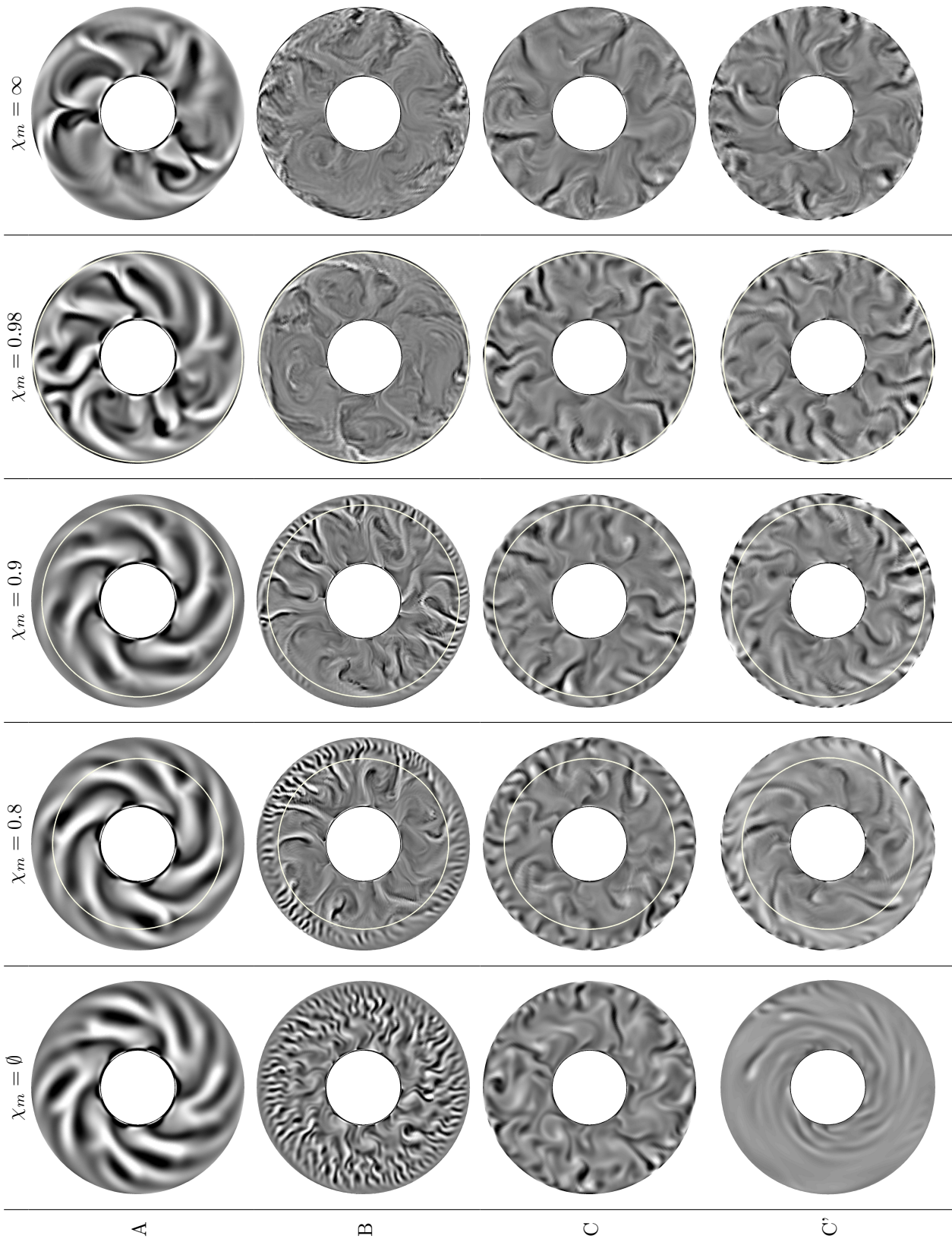


Figure 6: For the same snapshots as in figure 5, equatorial cuts of the axial vorticity, $\omega_z = \mathbf{z} \cdot (\nabla \times \mathbf{u})$. The colors represent the same values for each row but it is scaled between different sets. The circle with $r = r_m$ is drawn in white for each panel of the non-homogeneous electrical conductivity.

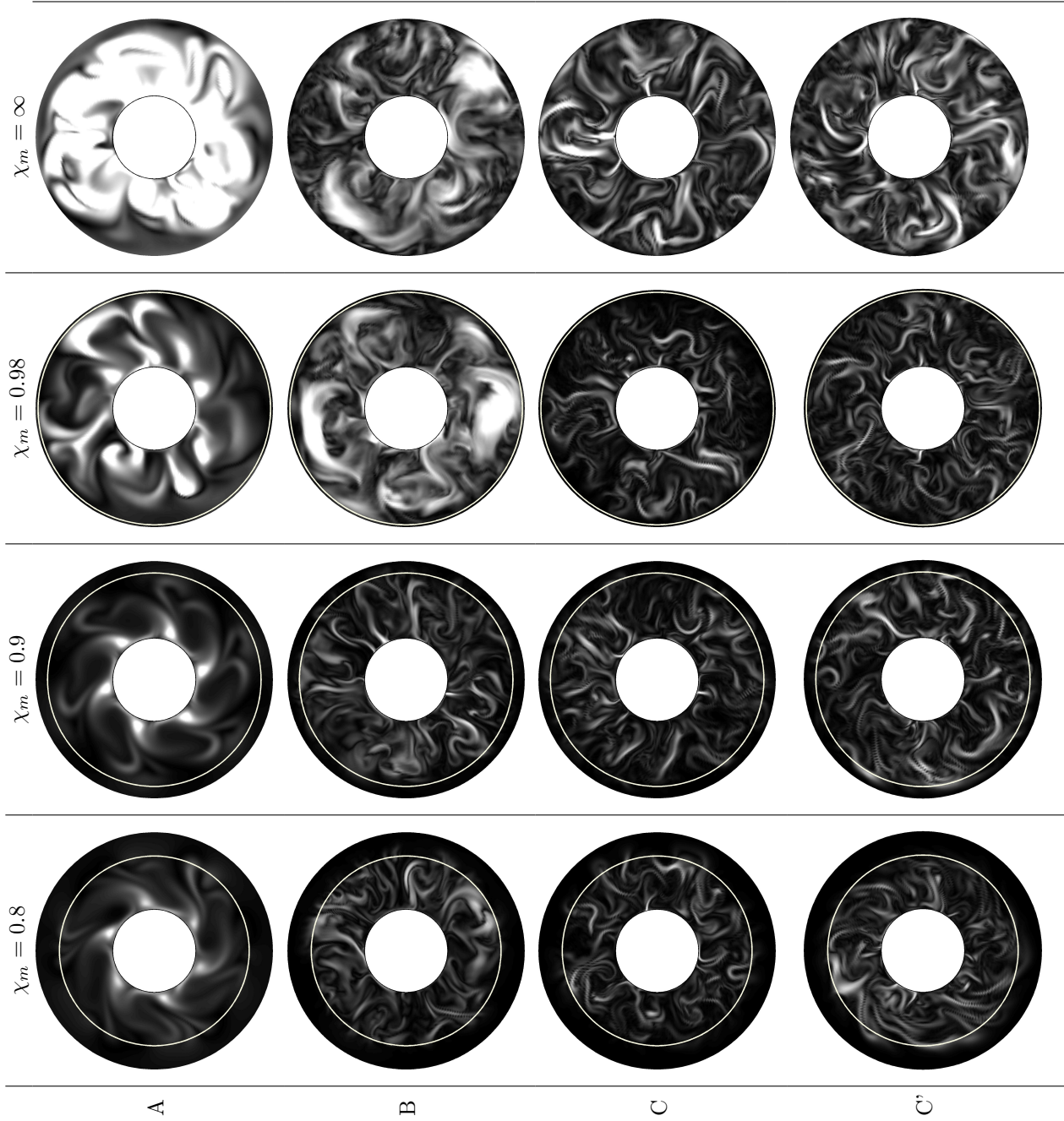


Figure 7: For the same time steps chosen for figures 5 and 6, snapshots of equatorial cuts of the magnetic field magnitude, $|\mathbf{B}|$ for the models in sets A, B, C and C' from top to bottom rows. From left to right, variable conductivity models with: $\chi_m = 0.8$ and $\chi_m = 0.9$, $\chi_m = 0.98$, and homogeneous non-zero electrical conductivity solutions. For the variable conductivity cases the circle of radius r_m is shown with a white solid line. The color scale is the same for each row but changes between sets, between 0 (black) and 1 (white) for set A, and 0 (black) and 15 (white) for sets B, C and C', in units of the Elsasser number.

mimic this prograde tendency and the magnetic field is regularly organized in azimuth with a dominant wave number of six. Runs $\chi_m = \infty$ and $\chi_m = 0.98$, do not show a clear prograde tilt with increasing radius, and have a higher dominant wave number than runs with lower values of χ_m . The correlation between cyclonic vortices and magnetic field maxima can be inferred for sets B, C and C', but it is not as evident as for set A. The length scale of the magnetic field decreases with decreasing χ_m .

The radial component of the magnetic field at the top of the simulated fluid is shown in figure 8.

The symmetry of the magnetic field reflects the symmetry of the internal flow. Similarly, as found by Heimpel et al. (2005), for quasi-geostrophic flows (such as those in set A) the thermal plumes generate Taylor columns in the flow that transport magnetic field lines, resulting in a magnetic field morphology that correlates well with the flow and the thermal structure. For the weakly forced system (set A), the case with a homogeneous electrical conductivity results in a dipolar dominated dynamo with low non-axisymmetric components. The variable conductivity cases, where the magnetic field generated by the strong dynamo region has diffused through the low electrical conductivity fluid, exhibit a dominant dipolar field as well, which is highly axisymmetric (more so than the homogeneous case). In contrast, the strongly forced systems (sets B, C and C'), with a more disorganized flow regime, result in non-axisymmetric fields with significant higher degree components.

There is an identifiable transition in flow and magnetic field morphology that corresponds to different values of the conductivity profile radius ratio χ_m . For cases with thick variable conductivity layers (low χ_m), thermal and flow fields resemble those of non-magnetic convection (see figures 5 and 6). In contrast, for relatively thin variable conductivity layers (high χ_m) result in flow and magnetic fields that closely resemble the homogenous conductivity ($\chi_m = \infty$) cases. Such transition may be identified in Table 1 as a large increase in the CMB Elsasser number, Λ^{CMB} , for increasing χ_m .

This transition in magnetic field morphology and magnitude corresponds as well to a change in the relative strength of Coriolis and Lorentz forces. Time averages of the Coriolis and Lorentz forces as a function of radius for sets B and C are shown in figures 9 and 10. The volume averages has been taken over cylinders of radius r that have a symmetry axis parallel to $\hat{\mathbf{z}}$. In set B, runs where Λ^{CMB} is large, the top of the core exhibits a balance between Lorentz and Coriolis forces, with the exception of the region included in the Ekman layer (i.e., the last three grid points at the top of the simulated volume). For set C, the Coriolis is balanced by Lorentz in $\chi_m = \infty$. For both sets of magnetic cases with low Λ^{CMB} , the sum of Lorentz, Coriolis and Reynolds stresses is completely dominated by the Coriolis force, which is balanced by viscous forces at the top of the core. In this set for the case with $\chi_m = 0.98$, it is hard to assess whether there is a balance between Coriolis and Lorentz forces or whether the Coriolis dominates.

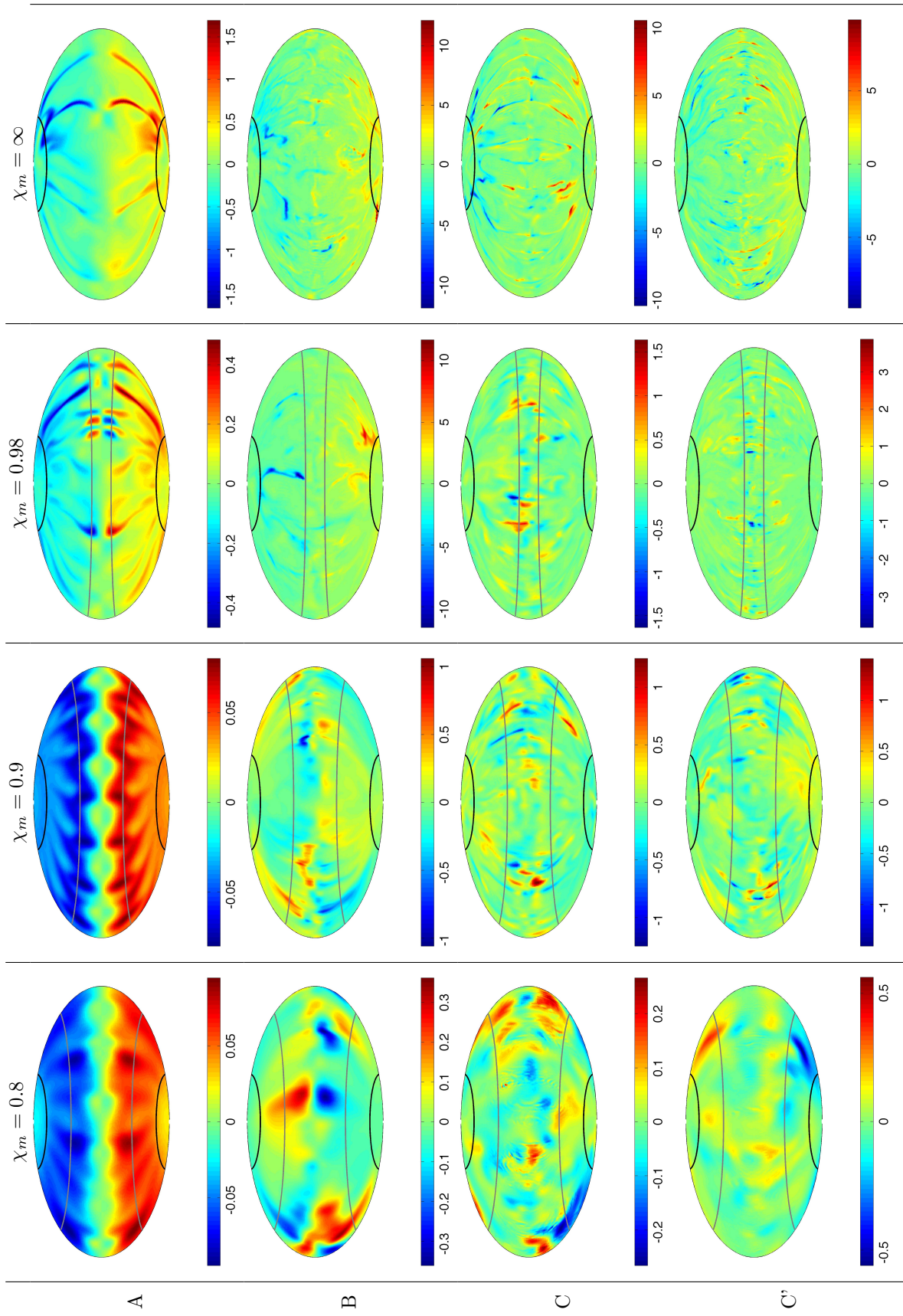


Figure 8: Images of the radial magnetic field at the top of the simulated fluid are shown in a Hammer projection. In each column snapshots for sets A, B, C and C', in columns left to right. The rows are organized in values of χ_m : 0.8, 0.9, 0.98 and ∞ from top to bottom. Red (blue) lines correspond to positive (negative) radial field in units of $\sqrt{\rho\mu_0\lambda_i\Omega}$. The projection of the tangent cylinder on the CMB is drawn here with a black solid line, and the projection of a tangent cylinder defined by the r_m is drawn in grey.

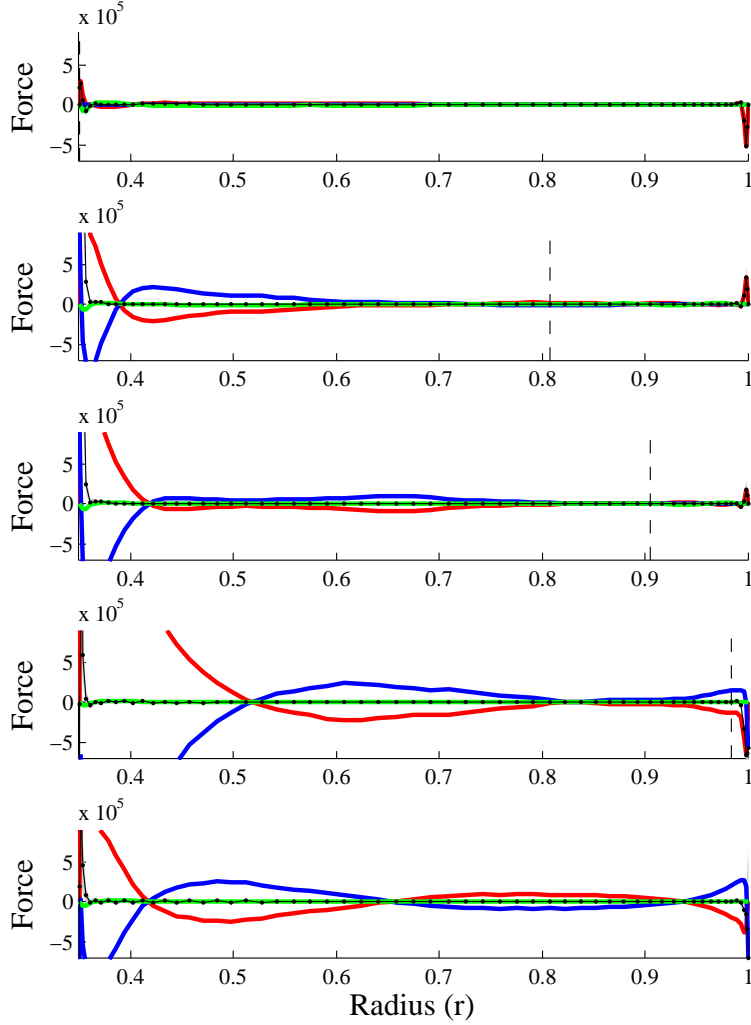


Figure 9: Time average of magnetic (blue) and Coriolis (red) forces as well as Reynolds stresses (green) over concentric cylinders at radii from r_i to r_o . In panels top to bottom increasing values of $\chi_m = 0, 0.8, 0.9, 0.89, \infty$ for set B. The sum of the Reynolds stresses, magnetic and Coriolis forces is shown in black dots and a solid black line with a grey shade showing the standard deviation of the time-average. Each panel has a vertical dashed line marking r_m .

6. Discussion

We find that the geometry and temporal variability of the magnetic field depends, to first order, on the spatial distribution of force balances. The de-

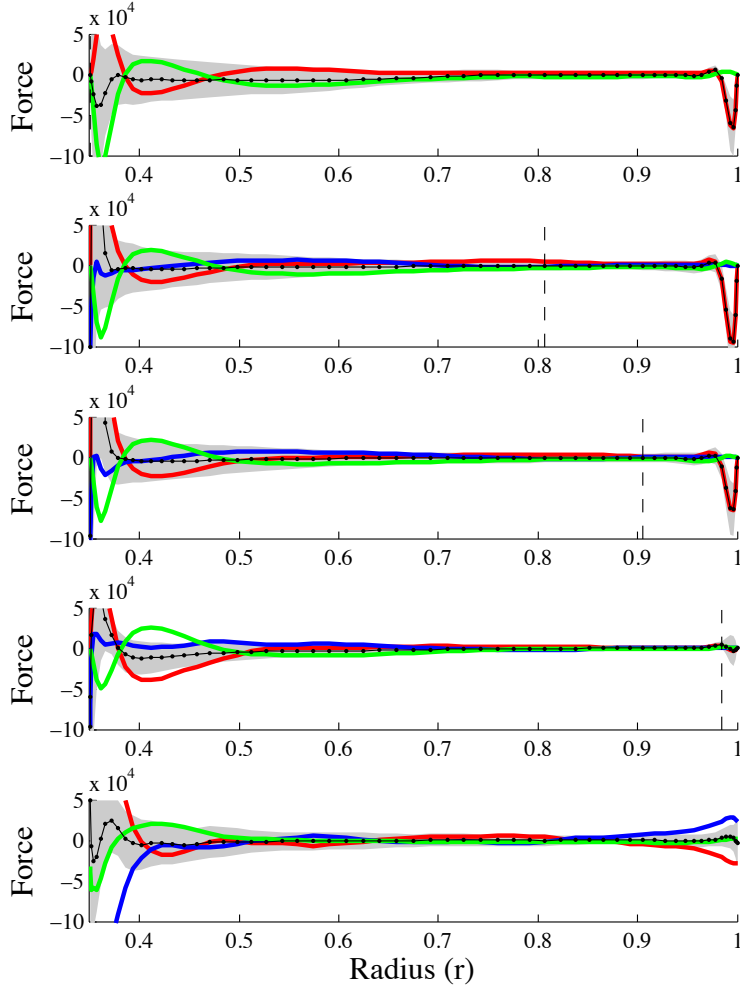


Figure 10: Similar to figure 9 but for set C. From top to bottom increasing values of $\chi_m = \emptyset, 0.8, 0.9, 0.98, \infty$. Reynolds stresses, magnetic and Coriolis forces are shown in green, blue and red respectively. The sum of them is shown in black dots joined by a solid black line.

crease of the electrical conductivity at the top of the simulated fluid results in significant changes in the resultant flow regime.

Christensen and Aubert (2006) reported an increase in the wave number with increasing Ra for non-magnetic convective runs, in agreement with experimental results (Aubert et al., 2001). They also point out that for magnetic cases the

correlation between mean wave number and Rayleigh number is incoherent, and they attribute it to a difference in force balances present in the magnetic cases versus the non-magnetic cases. In our models, for weakly forced cases, the prograde tilt of the Taylor columns caused by the spherical boundary is allowed for the cases where the Lorentz force is small at the boundaries (i.e., $\chi_m = 0.8$ and $\chi_m = 0.9$ in set A). Based on the snapshots shown here, e.g., Figure 6, there is indication that the characteristic length scale of the flow depends not only on the presence or absence of the Lorentz force but also on its spatial distribution. A reduction in the Lorentz force at the top boundary results in an overall change in the flow for sets A and C, where the convection becomes similar to that of the non-magnetic case. In set B the flow behaviour is different for high/low electrical conductivity regions changing the characteristic length scale of the flow as a function of radius.

The models with free-slip boundaries (set C') show that strong azimuthal flow in the non-magnetic case becomes weaker in regions of considerable electrical conductivity (see figure 5). This result is expected since strong zonal flows, can develop for free slip boundaries are damped by magnetic Lorentz forces. The Lorentz forces are proportional to the flow velocity and to the strength and volume of the conductive layer. In sets other than C', the resultant velocity is weaker. This is also expected, since strong zonal flows do not develop in no-slip boundary systems.

6.1. Boundary layers

It has been suggested in a recent paper that rotating convection can be controlled largely by the boundary layers (King et al., 2009). They compare the relation between: 1) the thermal boundary layer, $\delta_k \sim \frac{D}{2N_u}$, where $N_u = \frac{1}{4\pi r_i r_o} \frac{QD}{\rho c \kappa \Delta T}$ is the Nusselt number, c is the heat capacity, and Q is the total heat flow at the top boundary; and 2) the Ekman boundary layer $\delta_E \sim D\sqrt{E}$.

For non-magnetic rotating convection viscous and Coriolis forces govern the dynamics of the Ekman boundary layer. For convective dynamos there also exists the magnetic Lorentz force. The non-dimensional magnetic parameter analogous to the Ekman number is the Hartmann number $H = \left(\frac{B^2 D^2}{\mu_0 \lambda \rho \nu}\right)^{1/2}$ which is defined as the ratio of Lorentz to viscous forces. Associated with the Hartmann number is the Hartmann boundary layer. Inside the Hartmann layer viscous forces are important, while outside the layer magnetic forces dominate. The Hartmann layer thickness is $\delta_H = \frac{D}{|\mathbf{B}_\perp|} \sqrt{\mu_0 \lambda \rho \nu}$, where \mathbf{B}_\perp is the magnetic field normal to the surface (Potherat et al., 2002). Written in terms of the non-dimensional parameters used here,

$$\delta_H = D \sqrt{\frac{E}{\tilde{\sigma}_o \Lambda_r^{CMB}}}, \quad (14)$$

where $\tilde{\sigma}_o$ is a measure of the normalized electrical conductivity in the layer.

For this study the boundary layers are also affected by radially variable electrical conductivity. Decreasing the conductivity near the outer boundary

decreases the Lorentz force. A decreased electrical conductivity allows for a thicker boundary layer in which turbulent and/or molecular viscous forces are important. Figure 11 shows the time averaged boundary layer thickness of Hartmann, Ekman and thermal boundary layers as a function of χ_m . In sets

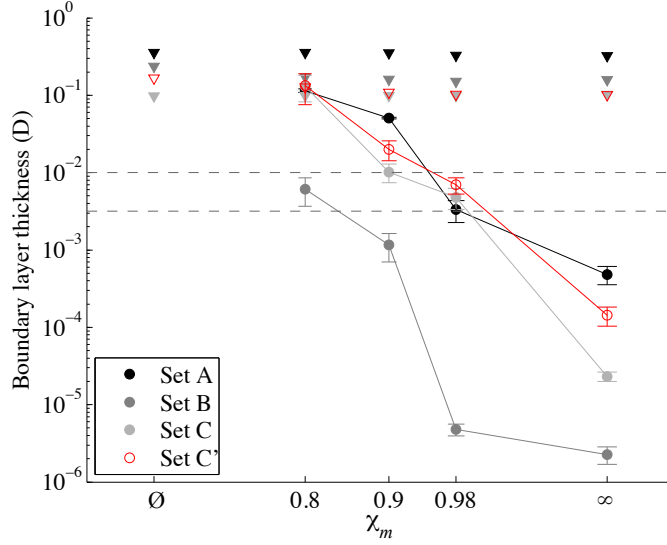


Figure 11: This figure shows the time-averaged boundary layer thickness in units of D as a function of χ_m . Triangles correspond to $\delta_k = \frac{1}{2N_u}$ (here the time variance is small and is not plotted), and circles correspond to $\delta_H = D \sqrt{\frac{E}{\sigma_o \Lambda_r^{CMB}}}$. Horizontal dashed lines for the Ekman boundary layer thickness are also plotted for sets A, C, and C' where $\delta_E = 10^{-2}$ and for set B where $\delta_E = \sqrt{10^{-5}}$.

A, C and C' the Ekman boundary layer thickness is $\delta_E = 10^{-2}$. When Lorentz forces do not influence the flow $\delta_H > \delta_E$. This is case for $\chi_m = 0.8$ in sets A, C and C' as well as and $\chi_m = 0.9$ in sets A and C' (see also Table 1). In the case of set B where $\delta_E \sim 0.0032$, $\delta_H > \delta_E$ only for $\chi_m = 0.8$, but for $\chi_m = 0.9$ $\delta_H = 0.001160$ is only a factor of 3 times smaller than δ_E . The transition in the flow behavior, found to be a consequence of the force balances at the top of the core, is correlated to the relation between the Ekman and Hartmann boundary layers.

When pressure gradients and gravity forces are balanced by the Coriolis force the flow is in a geostrophic balance. If the Coriolis is balanced by Lorentz forces, the flow is said to be in a magnetostrophic balance. Noting that we keep the thermal boundary layer constant for each set, and that δ_k is always large (see Table 1 and figure 11), we found that the relative thickness of Hartmann and Ekman layers results in force balances at the top of the core allowing for Lorentz or Coriolis forces to control the flow, resulting in magnetostrophic ($\delta_H < \delta_E$) or geostrophic ($\delta_E < \delta_H$) systems.

Inspection of the radial magnetic field (Figure 8), reveals the interplay between the Ekman and Hartmann boundary layers, and the variable conductivity layers near the outer boundary for the various cases. For set A, a relatively low Ra results in relatively weak magnetic field. Here the Hartmann layer thickness is similar to that of the low conductivity layer. For this set, we interpret the presence of strong surface radial magnetic field patches near the magnetic tangent cylinder to be indicative of the flow field, which tends to be deflected by a Hartmann layer topography (Potherat et al., 2002). For Set B, lower E and higher Ra , result in higher Λ and a δ_H that is thinner than the variable conductivity layer in the cases with $\chi_m = 0.8$ and $\chi_m = 0.9$. This results in high radial magnetic field patches at the outer surface outside the magnetic tangent cylinder (i.e., at lower latitudes than the intersection of the tangent cylinder with the outer surface).

In summary, for thick Hartmann layers, $\delta_H > \delta_E$, the flow is unaffected by the presence of magnetic forces and it may be controlled by the relation between Ekman and thermal boundary layers (King et al., 2009). However for a thin layer, $\delta_H \lesssim \delta_E$, the Lorentz forces dominate outside the Hartmann boundary layer while inside both, thermal and Ekman boundary layers. In our models, Ekman and Hartmann boundary layers define which force (Coriolis or Lorentz) is dominant just inside the region in which viscous forces are significant, so that the system follows a geostrophic or a magnetostrophic regime.

For rotating-convection, King et al. (2009) argue that for stress-free boundaries, there is a thermal Ekman layer which takes the place of the Ekman layer. Such layer would define the volume over which the rotation responds to density perturbations, modifying plume formation. They argue that the Ekman layer is dynamically important in stress-free systems. We find a transition in set C' for Λ^{CMB} to be between $\chi_m = 0.9$ and $\chi_m = 0.98$. This transition coincides with the change in the relation between δ_H and the traditional $\delta_E = \sqrt{E}$ (see figure 11). This is consistent with the relevance of δ_E in the dynamics with or without stress-free boundary conditions.

6.2. Planetary implications

Computational limitations preclude the use of accurate diffusion coefficients in modeling the Earth and planets. Furthermore, since we have carried out only a few cases that show the correspondence of strong and a weak external magnetic fields to boundary layers with different viscosities and electrical conductivity profiles, we are not in a position to attempt to scale our present results to conditions in planetary interiors. However, we can come to some preliminary conclusions using estimated planetary values of the Ekman and Hartmann layer thicknesses. Considering turbulent molecular viscous diffusion we can estimate the earth-like Ekman numbers of 10^{-9} and 10^{-15} , respectively, yielding Ekman layer thickness estimates of order 200 m and 0.2 m, respectively. Considering an Elsasser number at the top of Earth's core of 0.3 (Stevenson, 2003), the Hartmann to Ekman layer thickness of Earth may be estimated to be $\delta_H/\delta_E \sim 2$ where both, Ekman and Hartmann layers thickness are comparable, and a magnetostrophic core is expected.

Observations of Mercury’s magnetic field by Mariner 10 and recent MESSENGER flybys are consistent with a Hermean magnetic field that is weaker by about two orders of magnitude, but roughly similar in morphology to that of Earth (a moderately tilted axial dipole). Because Mercury is small, and its rotation rate is quite low (its sidereal day is 58.6 Earth days), its Ekman number is about 100 times greater than that of Earth. The Elsasser number scales like $\Lambda \propto B^2/\Omega$, Mercury’s Λ is less than that of Earth by a factor of roughly 1/500. Since the Hartmann layer thickness scales like $\delta_H \sim \delta_E/\sqrt{\Lambda}$ we obtain estimates for a Hermean Hartmann to Ekman layer thickness to be $\delta_H/\delta_E \sim 100$ where one expects a non-magnetostrophic flow.

7. Conclusions

In our models, the dynamo-generated magnetic field morphology and intensity are strongly affected by the relative strength of viscous, Coriolis and Lorentz forces near the outer boundary. The relative scale of Ekman and Hartmann boundary layer thicknesses is determined by an electrical conductivity gradient. For uniform electrical conductivity models Coriolis and Lorentz forces are typically of the same order, yielding a magnetostrophic balance. Low electrical conductivity near the top boundary can separate the Ekman-Hartman layer into a thin Ekman layer and a thicker Hartmann layer, resulting in changes of the detailed magnetic field morphology, and a large-scale external magnetic field that is relatively weak (see Table 1). Given the likelihood of a high concentration of light element in Mercury’s core, it is plausible that a low electrical conductivity layer is present near the core mantle boundary. This means that the dynamics of the boundary layers obtained in our models may be applicable to conditions in Mercury’s core. Our results imply that a low conductivity layer is consistent with Mercury’s weak observable magnetic field. However, while radially variable electrical conductivity is the mechanism studied in this paper, it is one of several models that can result in weak magnetic fields. With the anticipated arrival of the MESSENGER spacecraft in orbit, we will soon be in a position to use detailed mapping to better constrain the relative contributions of the various dynamical processes that generate Mercury’s global magnetic field.

Acknowledgements

The authors thank S. C. Solomon and J. M. Aurnou for helpful comments on the manuscript, Erik King for enlightening discussions, and the two anonymous referees for comments and questions that broadened the focus and improved greatly the quality of the manuscript. At DTM, NGP has been supported by the NASA MESSENGER project and by the NASA Planetary Geology and Geophysics Program, under contract NASW-00002 and grant NNX07AP50G, respectively. Computational resources were provided by the Western Canada Research Grid (Westgrid).

A. Symbols

Table 2: Symbols used throughout the document

Symbol	Description	units
a	polynomial exponent of the electrical conductivity function	
α	thermal expansion coefficient	K^{-1}
\mathbf{B}	magnetic field induction vector	$(\rho \mu_0 \lambda_i \Omega)^{1/2}$
c	heat capacity	$J (kg K)^{-1}$
χ	shell radii ratio	
χ_m	electrically conductive volume radii ratio	
δ_E	Ekman boundary layer thickness	D
δ_H	Hartmann boundary layer thickness	D
δ_k	thermal boundary layer thickness	D
E	Ekman number	
g	acceleration of gravity	$\nu^2 D^{-3}$
g_o	acceleration of gravity at the CMB	$\nu^2 D^{-3}$
H	Hartmann number	
κ	thermal diffusivity	$m^2 s^{-1}$
l_{max}	maximum spherical harmonic degree	
Λ	model-normalized Elsasser number	$\rho \mu_0 \lambda_i \Omega$
Λ^{CMB}	model-normalized CMB Elsasser number	$\rho \mu_0 \lambda_i \Omega$
Λ_r^{CMB}	model-normalized CMB radial field Elsasser number	$\rho \mu_0 \lambda_i \Omega$
λ	fluid electrical diffusivity	$m^2 s^{-1}$
$\tilde{\lambda}$	normalized electrical diffusivity	λ_i
λ_i	electrical diffusivity at the ICB	$m^2 s^{-1}$
M	magnetic energy in the fluid core	
M^a	axisymmetric magnetic energy in the fluid core	
M_o	magnetic energy at the CMB	
M_o^a	axisymmetric magnetic energy at the CMB	
μ_0	magnetic permeability of vacuum	$H m^{-1}$
Nu	Nusselt number	
ν	kinematic viscosity	$m^2 s^{-1}$
Ω	Angular momentum	s^{-1}
P	Pressure scalar	$\rho \nu \Omega$
Φ	toroidal potential	
Ψ	poloidal potential	
Pm^*	modified Magnetic Prandtl number	
Pr	Prandtl number	
Q	total heat flux at CMB	
Q^a	ratio axisymmetric dipole to total magnetic energy	
Q_o^a	ratio axisymmetric dipole to total magnetic energy at the CMB	
$\hat{\mathbf{r}}$	Unit vector in the radial direction	
ρ	Fluid density	$kg m^{-3}$
Ra	Rayleigh number	

Table 2: Symbols used throughout the document

Symbol	Description	units
Ra_c	critical Rayleigh number for the onset of convection	
Re	Reynolds number	
r_i	Shell internal radius	D
r_m	electrical conductivity transition radius	D
r_o	Shell external radius	D
σ	fluid electrical conductivity	m^{-2}s
$\tilde{\sigma}$	normalized electrical conductivity	σ_i
σ_i	electrical conductivity at the ICB	m^{-2}s
$\tilde{\sigma}_m$	normalized electrical conductivity at r_m	σ_i
$\tilde{\sigma}_o$	normalized electrical conductivity at the CMB	σ_i
T	Temperature scalar	ΔT
\mathbf{u}	flow velocity vector	νD^{-1}
$\hat{\mathbf{z}}$	Unit vector in the direction of the angular momentum	

References

- Al-Shamali, F., Heimpel, M. H., Aurnou, J. M., 2004. Varying the spherical shell geometry in rotating thermal convection. *Geophys. Astrophys. Fluid Dyn.* 98, 153–169.
- Alexandrakis, C., Eaton, D. W., 2007. Empirical transfer functions: Application to determination of outermost core velocity structure using SmKS phases. *Geophysical Research Letters* 34, L22317.
- Anufriev, A., Jones, C., Soward, A., 2005. The Boussinesq and anelastic liquid approximations for convection in the Earth’s core. *Physics of the Earth and Planetary Interiors* 152, 163–190.
- Aubert, J., Brito, D., Nataf, H., Cardin, P., Masson, J., 2001. A systematic experimental study of rapidly rotating spherical convection in water and liquid gallium. *Physics of the Earth and Planetary Interiors* 128 (1-4), 51–74.
- Birch, F., 1952. Elasticity and constitution of the Earth interior. *J Geophys Res* 57, 227–286.
- Braginsky, S. I., 1993. MAC-oscillations of the hidden ocean of the core. *J Geomagn Geoelectr* 45, 1517–1538.
- Braginsky, S. I., 2007. Formation of the stratified ocean of the core: A ternary alloy model. *Earth and Planetary Science Letters* 253, 507–512.
- Buffett, B., Garnero, E., Jeanloz, R., 2000. Sediments at the top of Earth’s core. *Science* 290, 1338–1342.
- Caracas, R., Verstraete, M., 2009. Fe-Si alloys in the lowermost mantle and the outer core. *EosTrans. AGU* 90 (22), Jt. Assem. Suppl. Abstract DI71A–07.

- Chandrasekhar, S., 1961. Hydrodynamic and Hydromagnetic stability. Dover.
- Christensen, U., Olson, P., Glatzmaier, G., Jan 1998. A dynamo model interpretation of geomagnetic field structures. *Geophysical Research Letters* 25 (10), 1565–1568.
- Christensen, U., Olson, P., Glatzmaier, G., 1999. Numerical modelling of the geodynamo: a systematic parameter study. *Geophys J Int* 138, 393–409.
- Christensen, U. R., 2006. A deep dynamo generating Mercury’s magnetic field. *Nature* 444, 1056–1058.
- Christensen, U. R., Aubert, J., 2006. Scaling properties of convection-driven dynamos in rotating spherical shells and application to planetary magnetic fields. *Geophys. J. Int.* 166, 97–114.
- Christensen, U. R., Wicht, J., 2008. Models of field generation in partly stable planetary cores: Applications to Mercury and Saturn. *Icarus* 196, 16–34.
- Clune, T., Elliott, J., Miesch, M., Toomre, J., Glatzmaier, G., Jan 1999. Computational aspects of a code to study rotating turbulent convection in spherical shells. *Parallel Comput* 25 (4), 361–380.
- Dormy, E., Cardin, P., Jault, D., 1998. MHD flow in a slightly differentially rotating spherical shell, with conducting inner core. *Earth and Planetary Science Letters*.
- Evonuk, M., Glatzmaier, G. A., 2004. 2D studies of various approximations used for modeling convection in giant planets. *Geophysical and Astrophysical Fluid Dynamics* 98, 241–255.
- Fearn, D., Loper, D., Jan 1981. The effect of composition upon the stratification of the core. *Geophys J Roy Astr S* 65 (1), 258–258.
- Featherstone, N. A., Browning, M. K., Brun, A. S., Toomre, J., 2007. Dynamo action in the presence of an imposed magnetic field. *Astron. Nachr.* 328, 1126–1129.
- Glatzmaier, G., 1984. Numerical simulations of stellar convective dynamos .1. the model and method. *J Comput Phys* 55, 461–484.
- Glatzmaier, G., Roberts, P., 1995. A 3-dimensional self-consistent computer-simulation of a geomagnetic-field reversal. *Nature* 377, 203–209.
- Gómez-Pérez, N., 2007. Planetary magnetic fields in the solar system: A numerical study of dynamo models. Ph.D. thesis, University of Alberta (Canada).
- Gómez-Pérez, N., Heimpel, M. H., Oct 2007. Numerical models of zonal flow dynamos: An application to the ice giants. *Geophys. Astrophys. Fluid Dyn.* 101 (5 & 6), 371–388.

- Guillot, T., 2005. The interiors of giant planets: Models and outstanding questions. *Ann. Rev. Earth Planet. Sci.* 33, 493–530.
- Hauck, S., Dombard, A., Phillips, R., Solomon, S., 2004. Internal and tectonic evolution of Mercury. *Earth and Planetary Science Letters* 222, 713–728.
- Heimpel, M., Kabin, K., 2008. Mercury redux. *Nature Geosci* 1, 564–566.
- Heimpel, M. H., Aurnou, J. M., Al-Shamali, F. M., Gómez Pérez, N., 2005. A numerical study of dynamo action as a function of spherical shell geometry. *Earth Planet. Sci. Lett.* 236 (1-2), 542–557.
- Jacobs, J. A., 1975. *The Earth's Core*. Vol. 10. Academic Press, London.
- Kageyama, A., Watanabe, K., Sato, T., 1993. Simulation study of a magnetohydrodynamic dynamo - convection in a rotating spherical-shell. *Phys Fluids B-Plasma* 5, 2793–2805.
- King, E. M., Stellmach, S., Noir, J., Hansen, U., Aurnou, J. M., 2009. Boundary layer control of rotating convection systems. *Nature* 457, 301–304.
- Kuang, W., Bloxham, J., 1997. An Earth-like numerical dynamo model. *Nature* 389, 371–374.
- Lister, J., Buffett, B., 1998. Stratification of the outer core at the core-mantle boundary. *Physics of the Earth and Planetary Interiors* 105, 5–19.
- Margot, J. L., Peale, S. J., Jurgens, R. F., Slade, M. A., Holin, I. V., 2007. Large longitude libration of Mercury reveals a molten core. *Science* 316, 710–714.
- McDonough, W. F., 2003. Compositional model for the Earth's core. In: Carlson, R. W. (Ed.), *The mantle and core*. Elsevier-Pergamon, Oxford.
- Moffatt, H., Loper, D., 1994. The magnetostrophic rise of a buoyant parcel in the Earth's core. *Geophys J Int* 117, 394–402.
- Nellis, W., 2000. Metallization of fluid hydrogen at 140 GPa (1.4 Mbar): implications for Jupiter. *Planetary and Space Science*.
- Poirier, J., 1994. Light elements in the Earth's outer core: A critical review. *Phys. Earth Planet. Int.* 85, 319–337.
- Potherat, A., Sommeria, J., Moreau, R., 2002. Effective boundary conditions for magnetohydrodynamic flows with thin Hartmann layers. *Phys. Fluids* 14 (1), 403–410.
- Sakuraba, A., Kono, M., 1999. Effect of the inner core on the numerical solution of the magnetohydrodynamic dynamo. *Physics of the Earth and Planetary Interiors* 111, 105–121.

- Solomon, S. C., McNutt, R. L., Watters, T., Lawrence, D. J., Feldman, W. C., Head, J. W., Krimigis, S. M., Murchie, S. L., Phillips, R. J., Slavin, J. A., Zuber, M. T., 2008. Return to Mercury: A global perspective on MESSENGER's first Mercury flyby. *Science* 321, 59–62.
- Stacey, F., Anderson, O., 2001. Electrical and thermal conductivities of Fe-Ni-Si alloy under core conditions. *Physics of the Earth and Planetary Interiors* 124, 153–162.
- Stacey, F., Loper, D., 2007. A revised estimate of the conductivity of iron alloy at high pressure and implications for the core energy balance. *Physics of the Earth and Planetary Interiors* 161, 13–18.
- Stanley, S., Bloxham, J., 2006. Numerical dynamo models of Uranus' and Neptune's magnetic fields. *Icarus* 184, 556–572.
- Stanley, S., Mohammadi, A., 2008. Effects of an outer thin stably stratified layer on planetary dynamos. *Physics of the Earth and Planetary Interiors* 168, 179–190.
- Stevenson, D. J., 2003. Planetary magnetic fields. *Earth Planet. Sci. Lett.* 208, 1–11.
- Stevenson, D. J., Jan 2008. Metallic helium in massive planets. *P Natl Acad Sci Usa* 105 (32), 11035–11036.
- Tanaka, S., 2007. Possibility of a low P-wave velocity layer in the outermost core from global SmKS waveforms. *Earth and Planetary Science Letters* 259, 486–499.
- Wicht, J., 2002. Inner-core conductivity in numerical dynamo simulations. *Physics of the Earth and Planetary Interiors* 132, 281–302.
- Wood, B., Walter, M., Wade, J., 2006. Accretion of the Earth and segregation of its core. *Nature* 441, 825–833.